Application of wave-equation migration velocity and Q analysis to the field data from the North Sea

Yi Shen

ABSTRACT

The Dolphin Geophysicals (Dolphin) multi-client field data acquired in the North Sea used in this study has attenuation problems. The area was under the influence of salt tectonics, producing two diapirs. Dolphin interpreted a gas chimney above one diapir, and a channel above the other. The gas chimney forms a migration pathway for the gas to leak and then to accumulate at the shallow position. The shallow gas gives rise to strong attenuation and low interval velocities in the gas area. The channel also has low velocities, and strong attenuation is associated with it. The objective of my study is to update the provided velocity model, especially at the gas and channel area, and to invert for the Q models to recover these two anomalies. Angle domain common image gathers after migration with the current interval velocity show that most of the events are curved down, indicating the current velocity is too high. Furthermore, both the migrated image and the angle gathers show that the events between 26,000 meters (m) to 28,000 m and 38,000 m to 42,000 m are wiped out below the two salt bodies. The attenuation anomalies above two salt bodies are the main reasons for the wiped-out image below. I first applied wave-equation migration velocity analysis to update the current velocity model. As a result, the velocity decreases in the gas and channel area. The angle gathers migrated using the updated velocity model are much more flattened, and the events above the top of salt in the migrated images are more coherent. Then, I applied wave-equation migration Q analysis to invert for the Q models. The estimated Q model shows that the two Q anomalies are recovered and match the interpretation. By using this Q model in seismic migration, I made the seismic events below the anomalies clearly visible, with improved frequency content and coherency of the events.

INTRODUCTION

Seismic attenuation, typically quantified by a parameter Q, is a notoriously challenging problem for reservoir identification and interpretation in the North Sea, where strong attenuation anomalies are present. Attenuation degrades the seismic image quality by decaying the image amplitude, lowering the image resolution, distorting the phase of events, and dispersing the velocity. These problems impede accurate image interpretation for hydrocarbon production and well positioning. The Dolphin's

multi-client field data acquired in the North Sea (CNS data) used in this study has such an attenuation problem. Gas chimneys and channels exist in the subsurface with strong attenuation and low interval velocity. These complexities reduce the amplitude and phase of deeper events, and essentially create a shadow zone over the salt body below and at the potential reservoirs, thus hampering accurate reservoir interpretation. Therefore, it is important to build a velocity model as accurate as possible. It is also valuable to understand and quantify the effects of these attenuation anomalies to create an accurate laterally- and vertically- varying attenuation model. The improvements in image quality using the derived model provide greater confidence for hydrocarbon exploration.

In my previous studies, I have shown the methodology and workflow to update the Q model using wave-equation migration Q analysis (WEMQA) (Shen et al., 2013, 2014, 2015; Shen* et al., 2015). I have also included the velocity inversion using wave-equation migration velocity analysis (WEMVA) (Sava and Biondi, 2004; Zhang and Biondi, 2013) into the Q inversion workflow to update both the velocity and Q models (Shen, 2015). I have demonstrated the successful application of WEMQA combined with WEMVA on a modified synthetic SEAM model (Shen, 2015). In this study, I continuously use this workflow (Shen, 2015) to build velocity and Q models for this field data to recover the gas and channel; and therefore to produce an improved seismic image.

In this paper, I first give an overview of these field data. Second, I present my preprocessing workflow to prepare the data for the later analysis. Third, I apply WEMQA combined with WEMVA to update the current velocity model and to invert for the Q models to recover the Q anomalies.

DATA DESCRIPTION

The CNS data is acquired using a marine-towed streamer seismic survey in the North Sea. The data provided by Dolphin for this research contain 28 sail lines, which were acquired by three vessels. The streamer configurations for the survey of three vessels are similar. Figure 1(a) shows the streamer configuration for the survey of one of the vessels. This vessel has 10 streamers. Each streamer is 6,000 m long, and the separation between the neighboring streamers is 75 m. The source was configured with two shots, in a flip-flop mode with a shot interval of 25 m. The source separation was 37.5 m. The streamer depth for all the survey was 30 m, and the source depth was 6 m, as shown in Figure 1(b). As a result, both the receiver-side ghost notch and source-side ghost notch are able to be calculated using equation $f = c/2d$, where f is the frequency of the first ghost notch, c is the water velocity of $1500m/s$ and d is the streamer/source depth. The results show that the receiver-side ghost has its first notch at 25 Hz, and the source-side ghost has its first ghost notch at 125 Hz.

The CNS data have strong attenuation anomalies. The depth slice provided by Dolphin in Figure 2 highlights the areas with the strongest gas chimneys and strongest

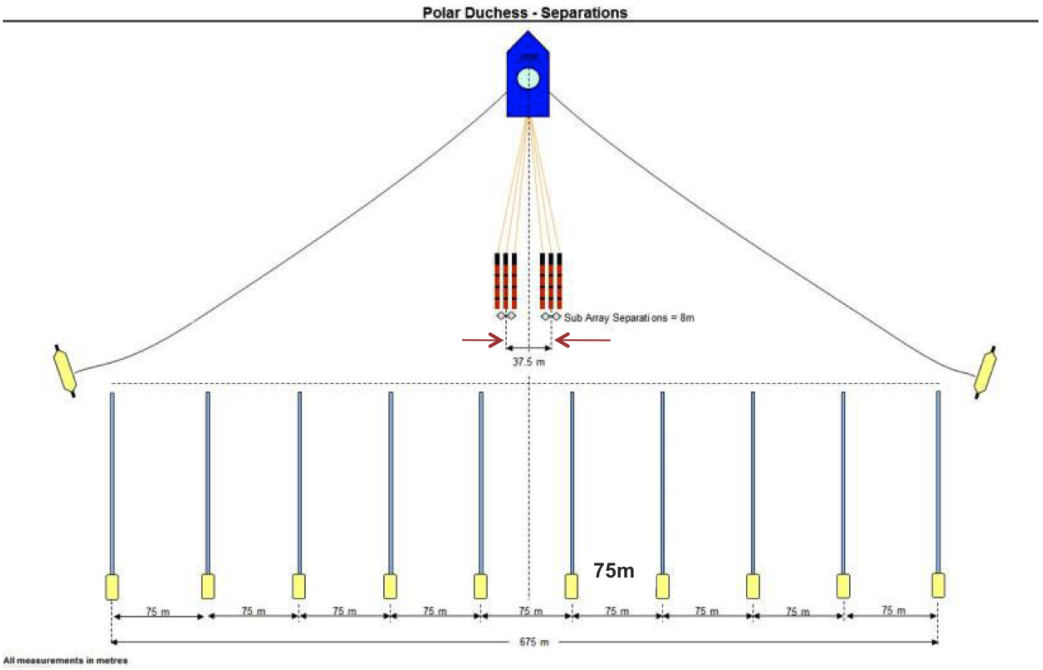

(a)

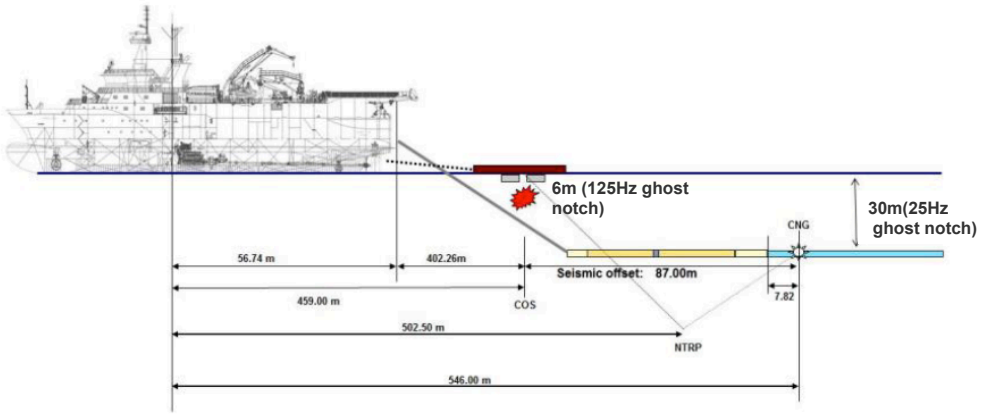

(b)

Figure 1: (a) The streamer configuration for the survey and (b) the boat configuration of one of the three vessels that are involved in these field data acquisition. [**NR**]

channel effect. The depth slice in Figure 2 does not cover the entire survey, but it covers the most complex area for the study of these anomalies. According to the interpretation by Dolphin, attenuation appears stronger from gas chimneys than from the channels. Attenuation from the gas on the right dome of the slice is stronger than the one on the bottom left dome of the slice. The channel at the top left of the slice shows low velocities, and there might be Q anomalies with it, although exhibiting less attenuation. The part of the survey provided by Dolphin for this study covers the left gas chimney and channel but does not include the anomaly on the right of the slice.

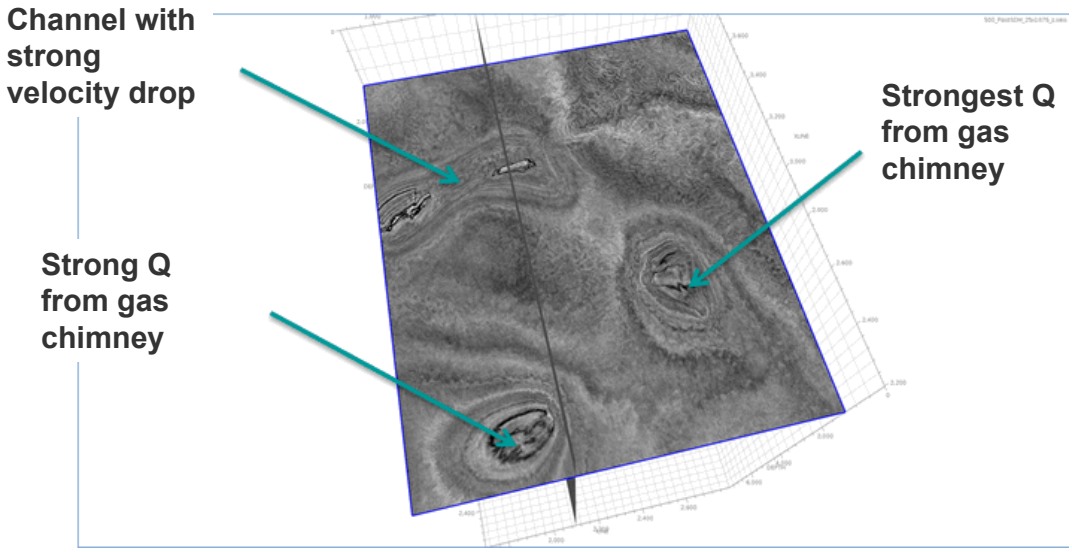

Figure 2: A depth slice provided by Dolphin that highlights the areas with the strongest anomalies associated to gas chimneys and channel. North is upward. [**NR**]

PREPROCESSING

Coordinates manipulation

The original coordinates of source and receiver of CNS data provided by Dolphin are not regularly sampled along neither inline nor crossline direction, and they are in a rotated Cartesian coordinate system. First, I shifted the origins of the coordinates and rotated the tilted coordinates to align the X–axis with the inline direction and the Y–axis with the crossline direction. The rotated and shifted coordinates of source and receivers are shown in Figure 3. Aligning the processing grid axes with the acquisition inline and cross-line directions makes it easy to bin the seismic shot gathers to the regularly sampled data grid that I create. Then, I regularized the grids of the source and receiver coordinates using the parameters shown in Table 1, facilitating subsequent data processing.

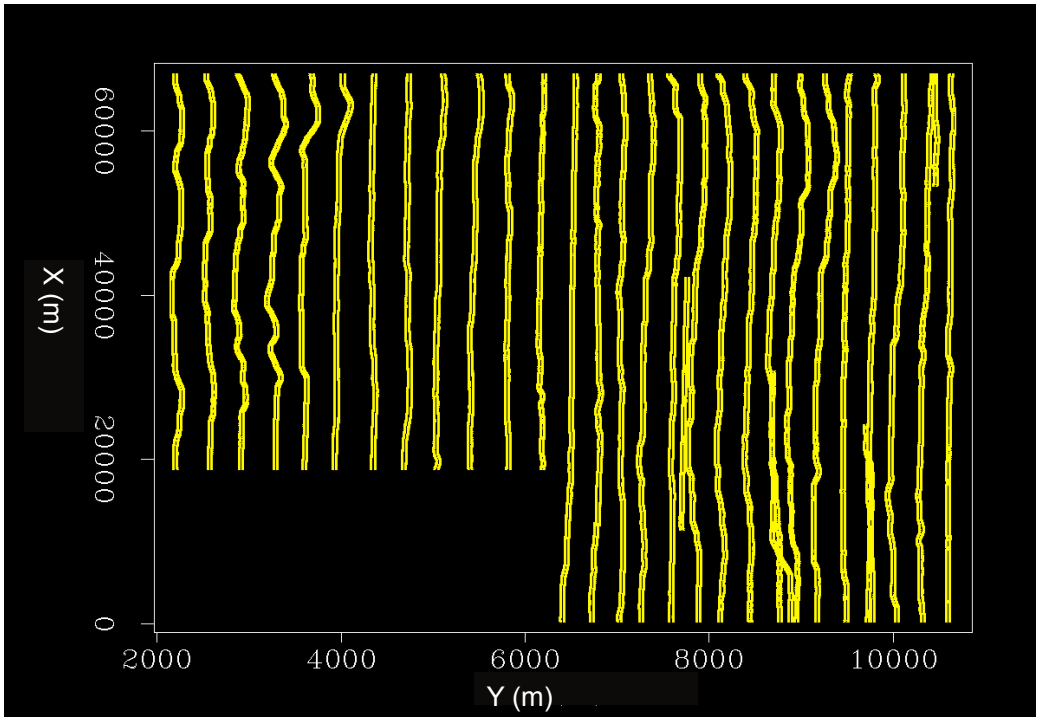

(a)

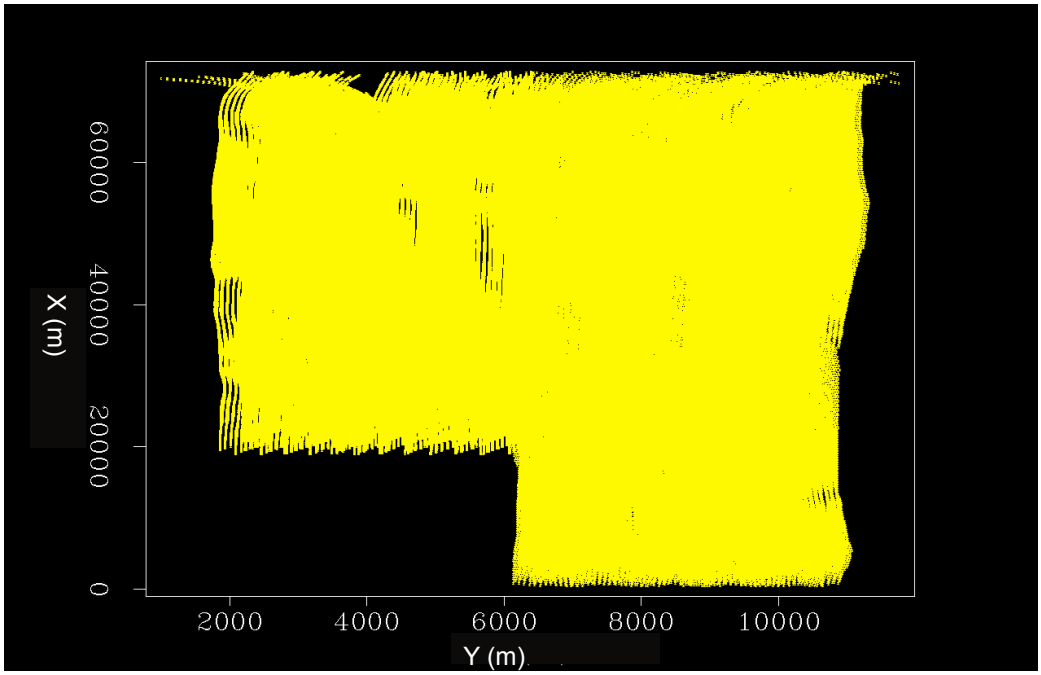

(b)

Figure 3: Rotated and shifted coordinates of (a) shots and (b) receivers. [**NR**]

Table 1: The parameters used for regularizing the grids

Keys	number	origin [m]	spacing [m]
Receiver at crossline (Y)	10	-337.5	75
Receiver at inline (X)	240	50	25
Source at crossline (Y)	28	2100	300
Source at inline (X)	1239	230	50

Denoise, Demultiple, Debubble and Deghost

This data is strongly influenced by swell waves that propagate along the interface between water and air. Such noise can also be identified in the FK domain of the data. Figure 4(a) shows a common offset gather at offset=300 m. The vertical strips in the common offset gather are the low-frequency noise that is generated by the swell noise. Figure 5(a) shows the same common offset gather of Figure 4(a) in the FK domain. The horizontal strip around 0 Hz frequency corresponds to the low-frequency noise. Therefore, I use a low-cut filter at 2 Hz to remove such noise. Figure 5(b) shows the common offset gather in the FK doamin after filtering. The result in the physical domain is shown in Figure 4(b). Notice the virtual absence of vertical strips, which means the swell noise is removed.

Beside the swell noise, these data are also contaminated by water-bottom multiples, salt-interval multiples, bubbles from the airguns, and the ghost described in the previous section. These noises copy events, e.g. water bottom reflection, at a periodic spatial interval. I used a gapped Preconditioning Error Filter (PEF) to remove such repetitive patterns (Clarebout and Fomel, 2014). Figure 6(a) and 6(b) are the windowed common offset gather at offset=300 m before and after a gapped PEF being applied, respectively. The yellow arrows show the bubbles, ghosts and multiples in Figure 6(a). Such events, of which the locations are also indicated by yellow arrows in Figure 6(a), are partially removed. Figure 7(a) and Figure 7(b) show a representative shot gather before and after a gapped PEF being applied, respectively. Figure 7(a) shows the bubbles, ghosts and multiples that are pointed by the yellow arrows. The event marked as repetitive event is still unknown to me, which may be a result of a wave bouncing from the back of the boat. The locations of these marked events are removed from Figure 7(b) after a gapped PEF being applied. The events The spectra of Figure 7(a) and Figure 7(b) are compared in Figure 8. The first receiver-side ghost notch is flattened by the preprocessing with a gapped PEF. The noisy wiggles can be observed at the high frequencies in Figure 8, because PEF tries to flatten the spectra and therefore boosts the high frequency noise.

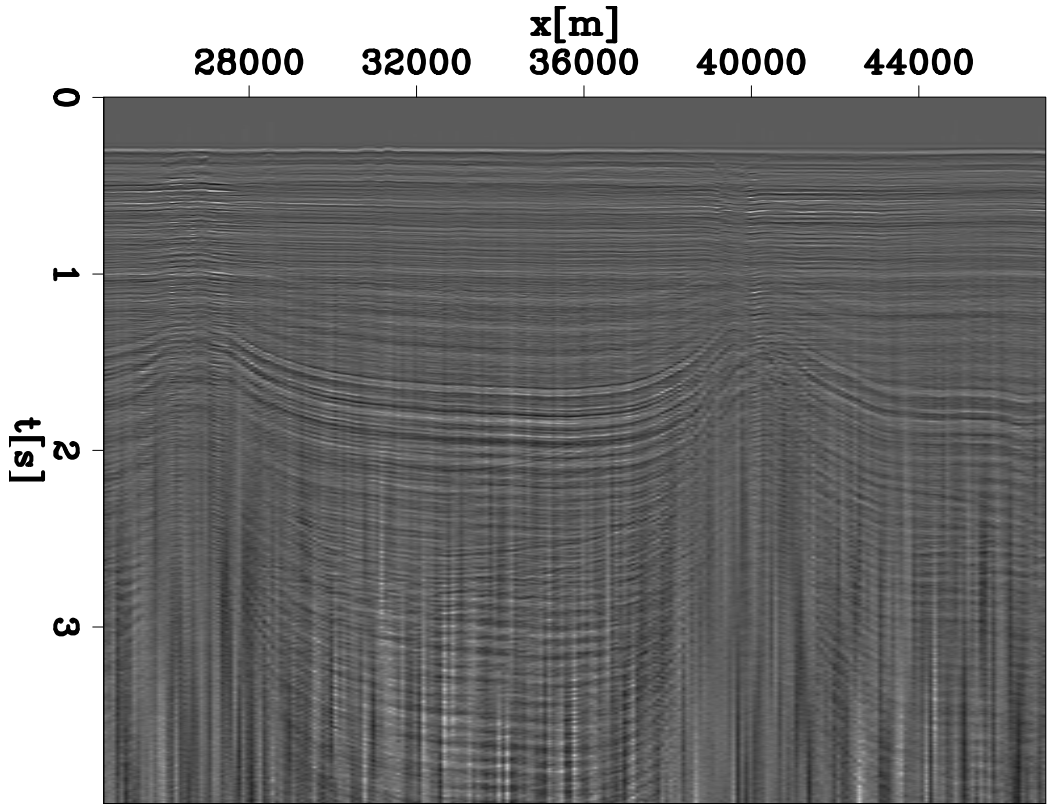

(a)

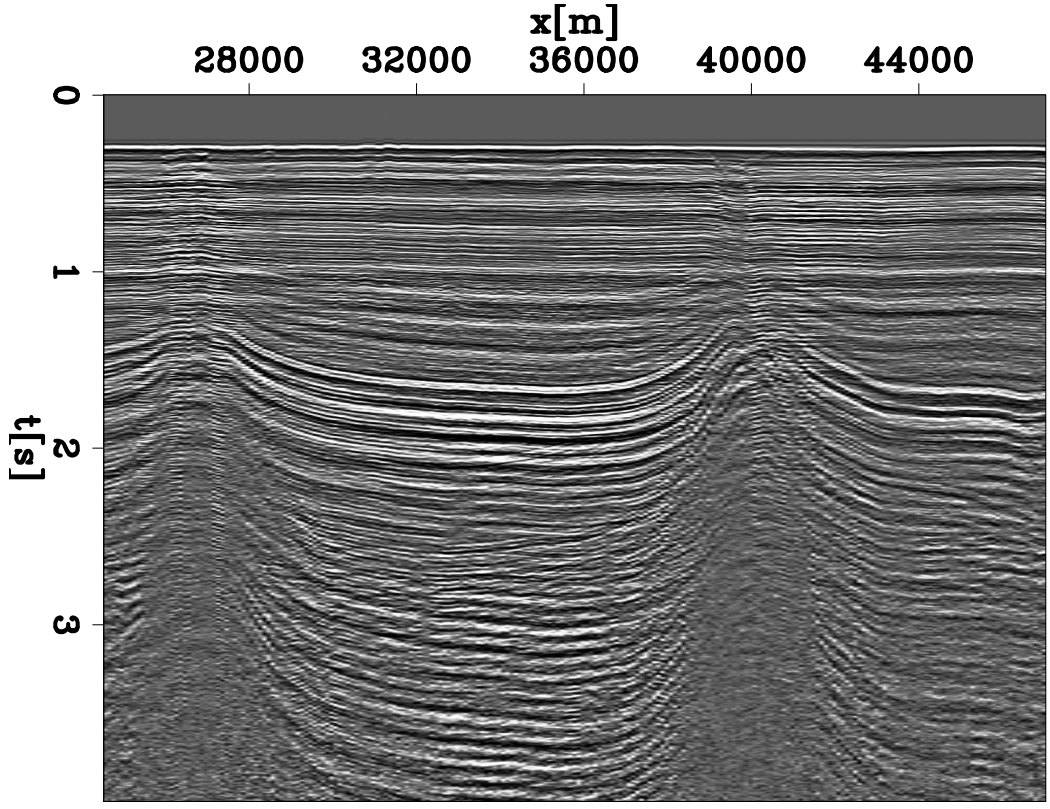

(b)

Figure 4: Common offset gather at offset=300 m: (a) before denoise; (b) after denoise. [**CR**]

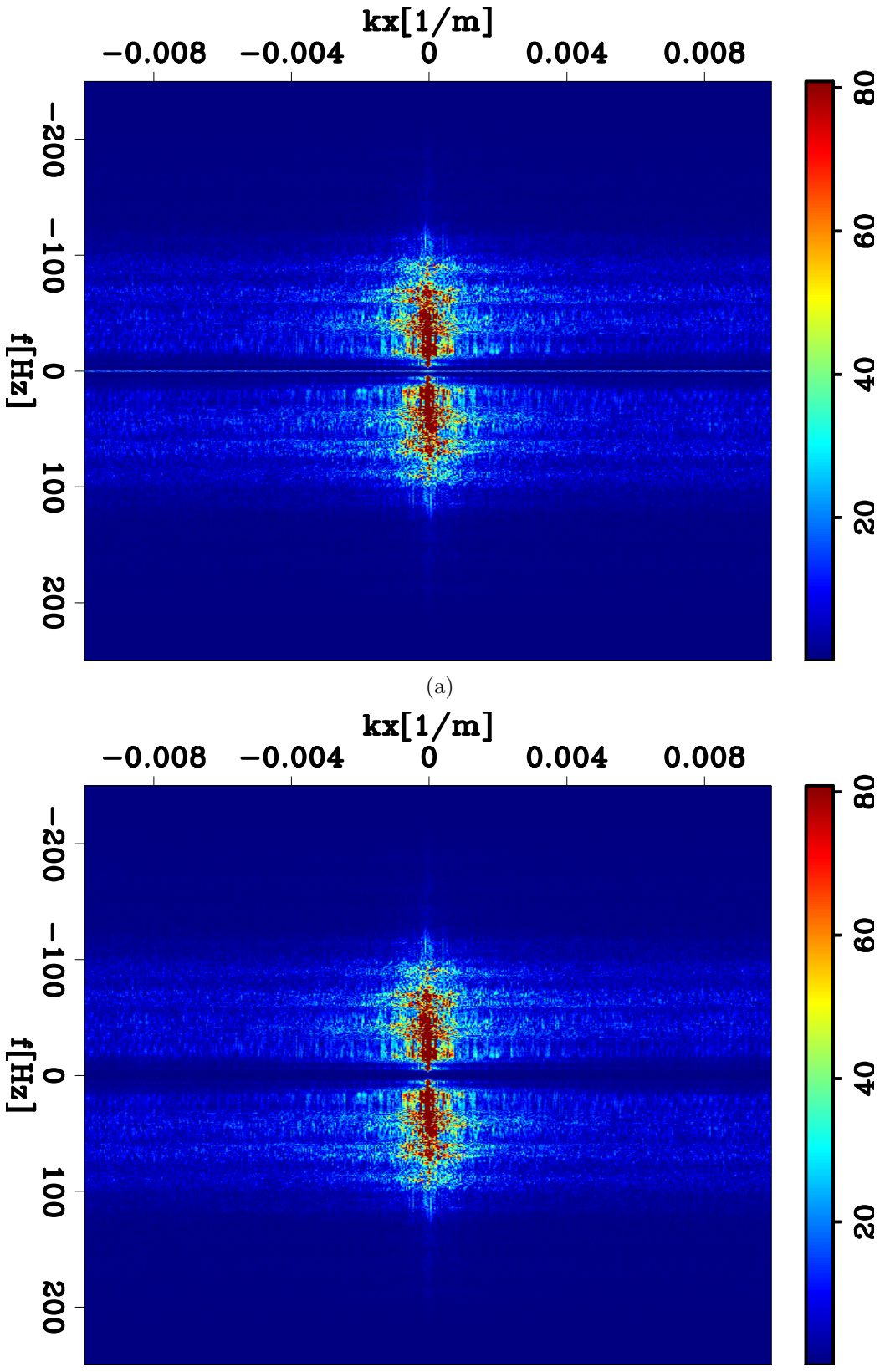

Figure 5: FK domain transformed from the common offset gather at offset=300: (a) before low-cut filter being applied; and (b) after low-cut filter being applied. [**CR**]

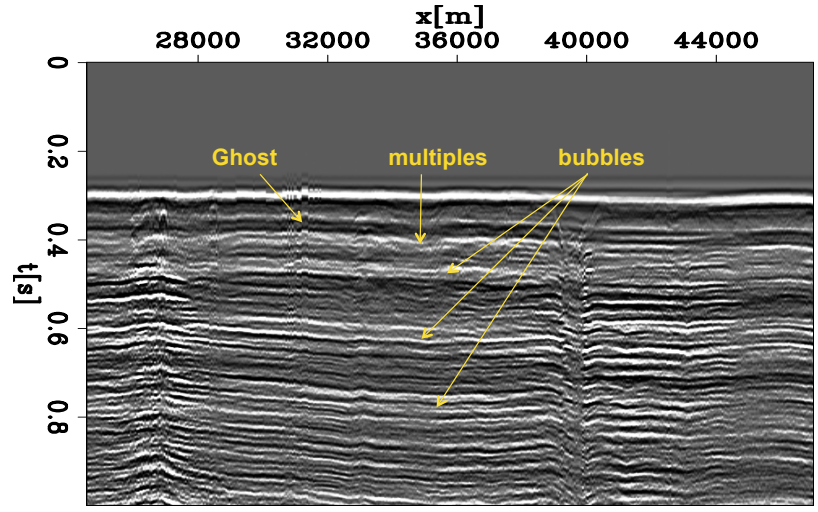

(a)

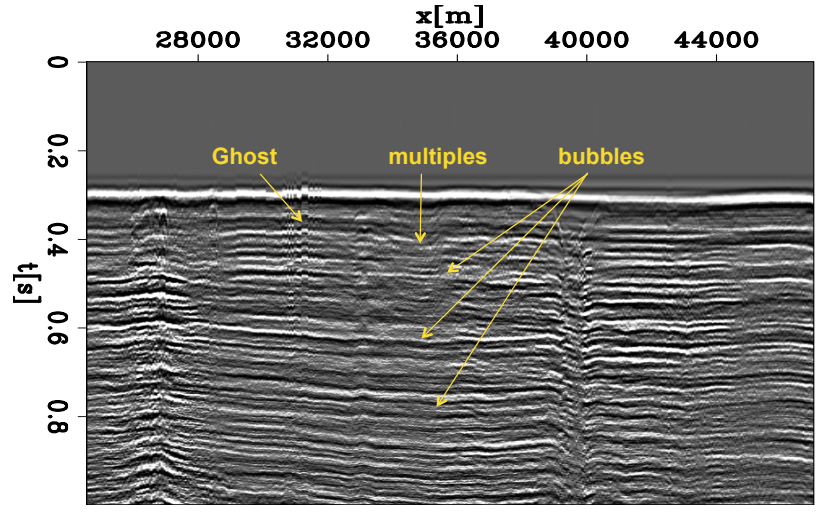

(b)

Figure 6: Windowed common offset gather at offset=300 m: (a) before processed with a gapped PEF; (b) after processed with a gapped PEF. The marked events are removed. [**CR**]

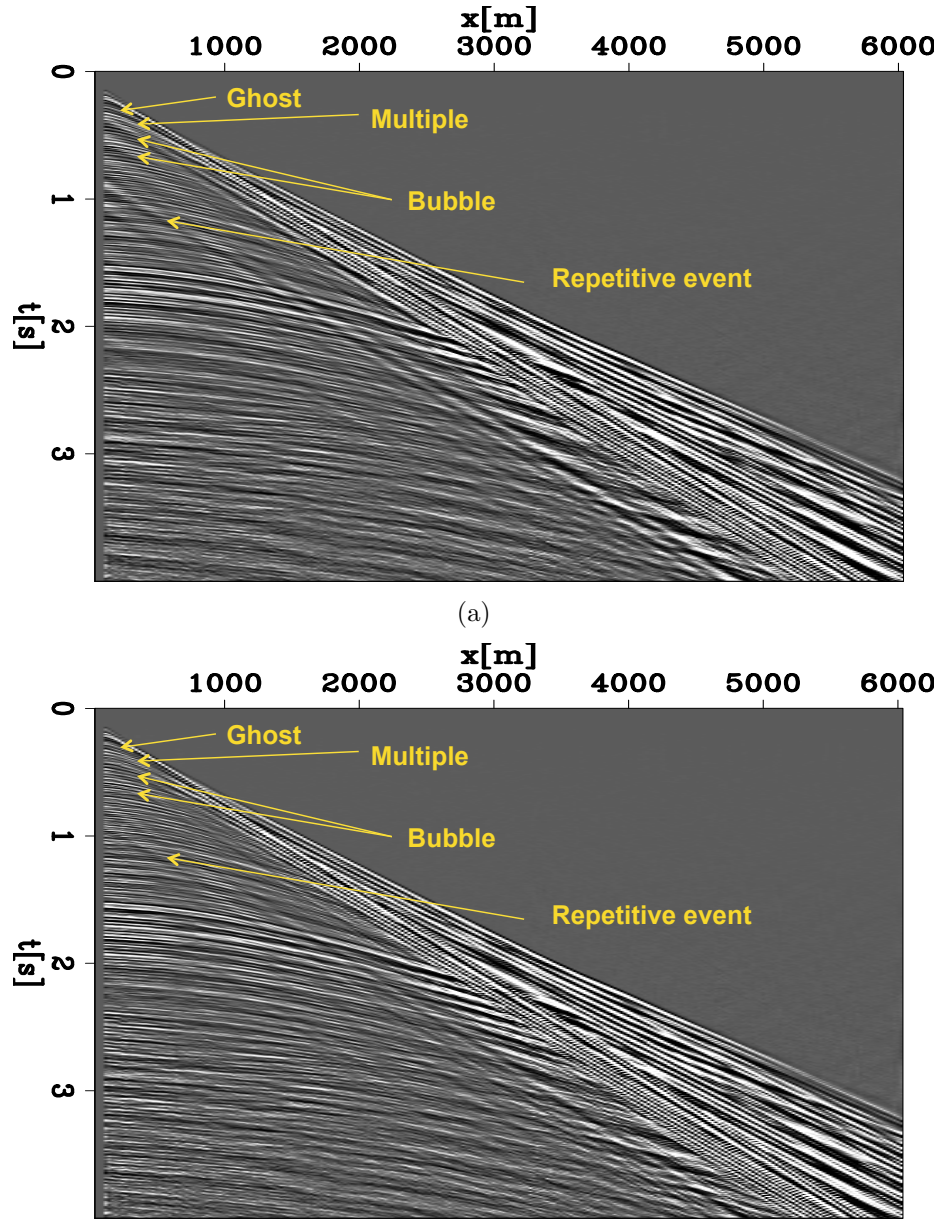

Figure 7: Shot gather at inline=24,580 m, crossline =7,500 m: (a) before processed with a gapped PEF; (b) after processed with a gapped PEF. The marked events are removed. [**CR**]

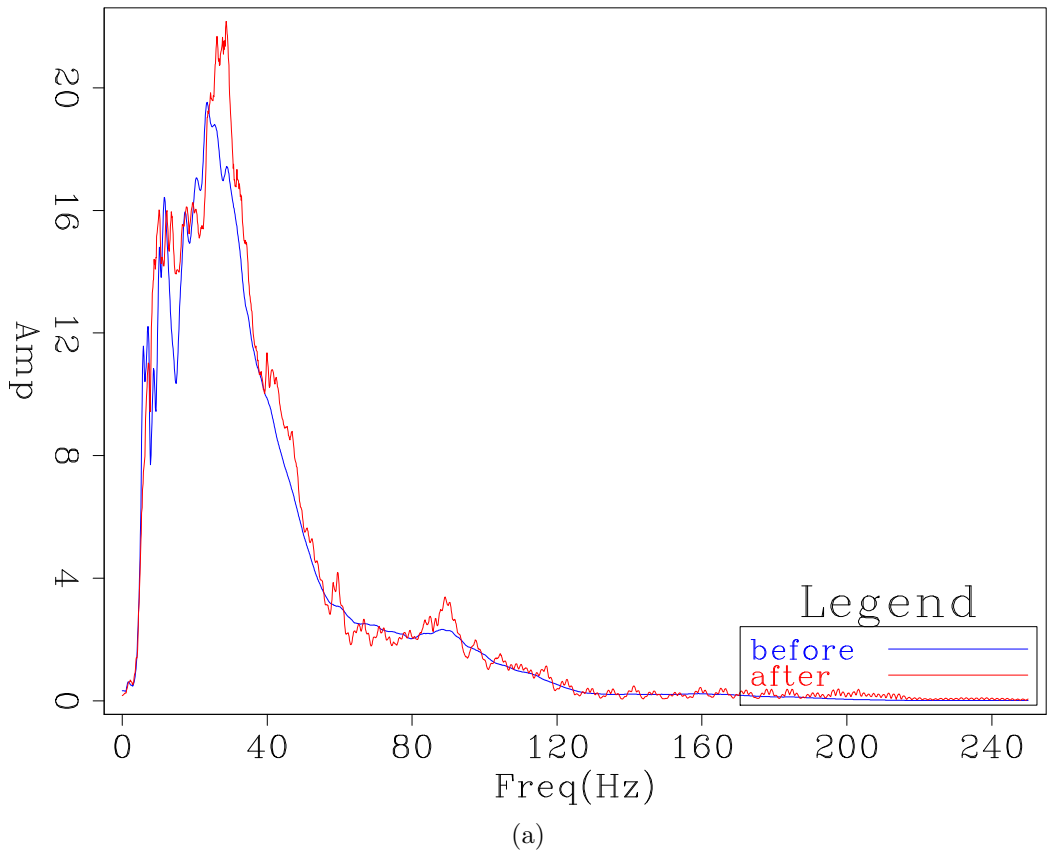

(a)

Figure 8: The spectra of Figure 7(a) and Figure 7(b). [**CR**]

TWO-DIMENSIONAL VELOCITY AND Q ESTIMATION

For the model building for this field study, I first focused the analysis on one representative two-dimensional (2D) section in order to set a proper inversion workflow and the corresponding parameter set for this particular dataset, and thus better prepare the road to 3D field inversion. In this report I show the results for the 2D inversion only. This 2D section is at the crossline 7,500 m, which passes through the left-side gas chimney and the left channel as shown in Figure 2. Figure 9 is the 2D slice of the 3D depth NMO interval velocity model provided by Dolphin at the crossline of 7,500 m, as an initial velocity model for the inversion. The velocity model shows a salt body with two diapirs, and a high-velocity layer above the salt body. Such layer acts as a potential cap layer. A gas chimney constitutes a migration pathway for the trapped gas that leaks and accumulates at the shallow position above the left diapir. The shallow gas presents low velocity and strong attenuation. Therefore, the velocities shown in Figure 9 at the shallow position above the left salt domes are slower than the surrounding areas. The area above the right salt domes also has slow velocities as shown in Figure 9, because of the presence of a low-velocity channel that as interpreted by Dolphin. Because Dolphin has not provided the Q model, the initial Q model for the inversion is set to be homogeneous with a value of 500.

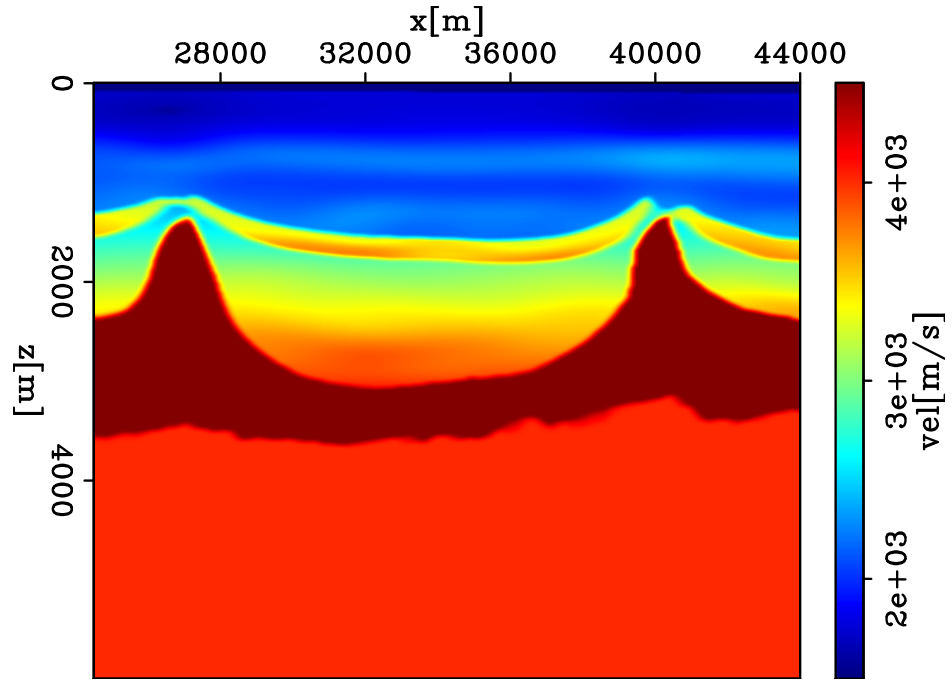

Figure 9: A 2D slice of the 3D depth NMO interval velocity model provided by Dolphin at the crossline of 7500 m, which passes through the left-side gas chimney and the left channel as shown in Figure 2. [**CR**]

Figure 10 is the migrated image using one-way wave-equation migration (Shen et al., 2013, 2014) at zero subsurface offset using the initial velocity model and the initial Q model. The migration frequency range is from 0.8 Hz to 50 Hz. The spacing

of the imaging grid used is 25 m in X by 25 m in Y by 10 m in Z. The salt body with two domes ($x = 26,000$ m to $28,000$ m and $x = 38,000$ m to $42,000$ m) is well imaged. The bright spots above the left and right salt peaks are the shallow gas and channel, respectively. These two regions have strong sand-shale impedance contrasts and thus their seismic reflection amplitudes are strong, which results in bright spots. The events below these two spots are wiped out. The attenuation caused by the shallow gas and channel is the main reason for the dimming region below. The dimming image at the boundary ($x < 25,000$ m and $x > 43000$ m) are tapered by the boundary condition in the migration. Figure 12 shows 10 representative Angle Domain Common Image Gathers (ADCIGs) of this migrated image using the initial models. The events in the ADCIGs are not flat but curved down, thereby indicating the velocity is too high. Angle gathers with midpoints close to the attenuation anomalies, e.g., ADCIGs at $x = 27$ km and $x = 41$, have lower amplitudes.

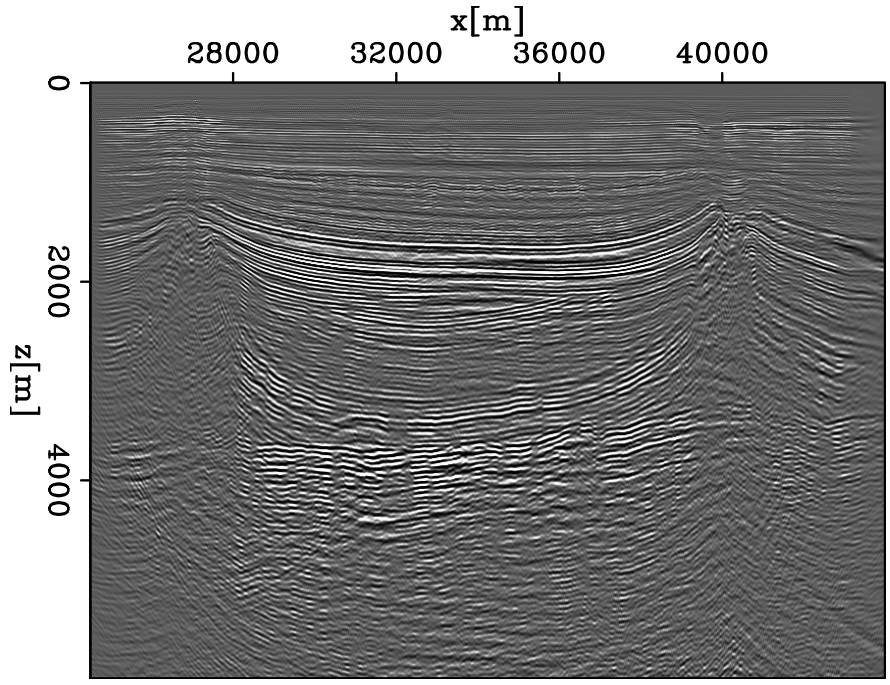

Figure 10: The migrated image at zero subsurface offset using the initial velocity model and the initial Q model. [**CR**]

I ran the velocity and Q inversion using the workflow described in my previous work (Shen, 2015) for 40 iterations. The optimization scheme described by Shen (2015)contains two objective functions: (1) one mainly for velocity updates, and (2) the other mainly for Q updates. Such scheme employs a weighting parameter β to balance these two functions. The previous study (Shen, 2015) shows that an error in velocity can cause significant error in the Q inversion results. The conspicuously curved-down events in the ADCIGs (Figure 12) indicate a significantly velocity error, therefore I focus on the velocity updating at the early iterations until the velocity error is significantly reduced. I update the Q model at the later iterations. In this

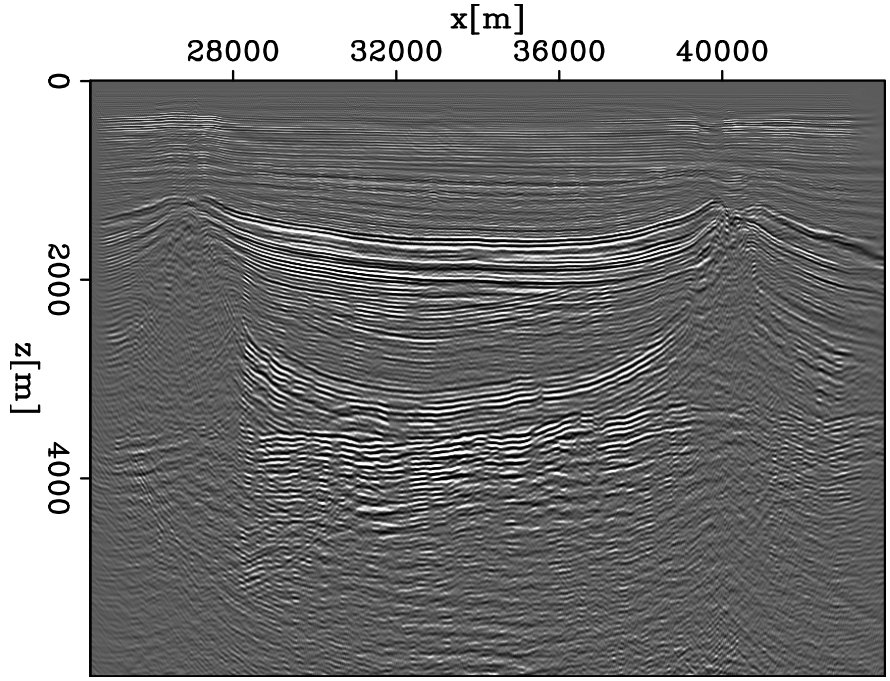

Figure 11: The migrated image at zero subsurface offset using the updated velocity model and the initial Q model. [**CR**]

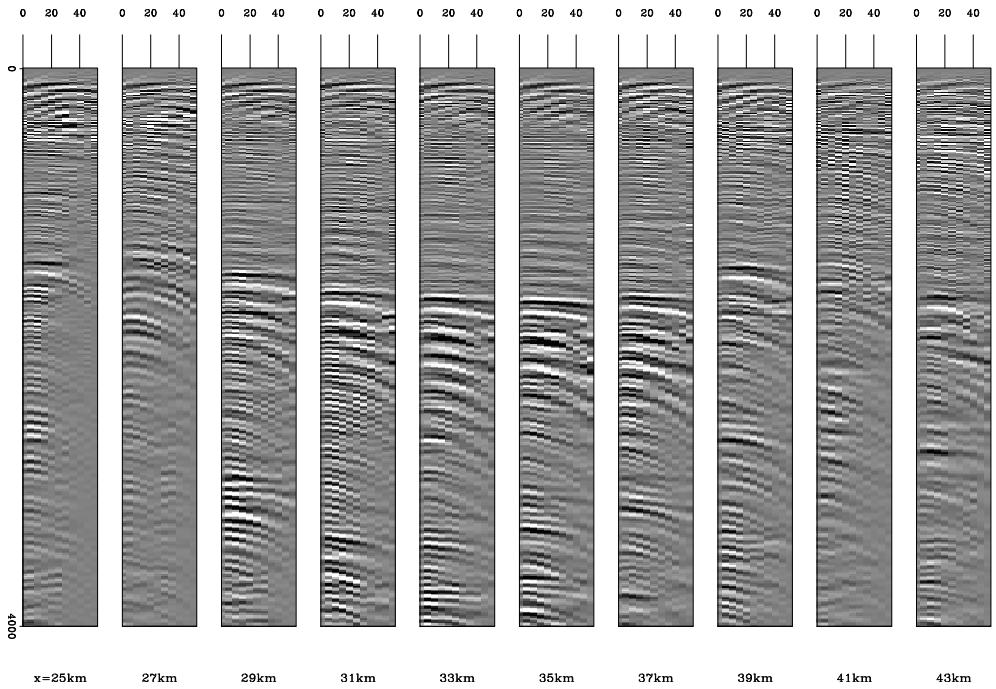

Figure 12: The ADCIGs using the initial velocity model and the initial Q model. [**CR**]

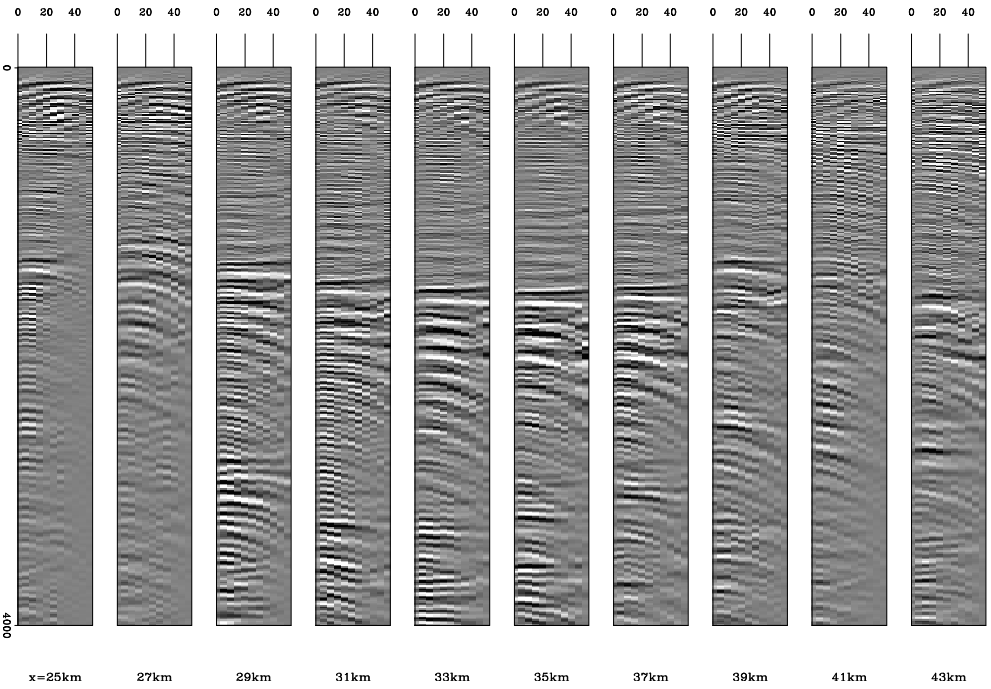

Figure 13: The ADCIGs using the updated velocity model and the initial Q model. [**CR**]

inversion, I set the weighting parameter β to be small (10^{-10}) to mainly estimate velocity during the first 20 iterations, and set β to be large (10^{10}) to mainly focus on Q estimation during the final 20 iterations.

I chose stack power of the migration image as the objective function for velocity updates. This method maximizes and therefore focuses the energy at the zero subsurface offset of the migrated image. Its low computational cost makes the application feasible for the later 3D inversion running in the computer resources of academic institutes. Figure 14 shows the velocity gradient of the first iteration of the inversion, in which the sign is opposite of the searching direction. The gradient shows the updates are strong around the shallow gas and the channel region and aims to decrease the velocity. Figure 15 is the updated velocity after 20 iterations. Compared to the initial velocity in Figure 9, the shallow velocity becomes slower, and the shallow low-velocity zone (above 500 m) becomes thicker. The decreases of the shallow velocity intend to push the events in ADCIGs upward and therefore flatten those events. The velocity drops more significantly above the salt domes, as shown in Figure 15, corresponding to the low-velocity anomalies of shallow gas and channel.

Figure 11 is the seismic image at zero subsurface offset migrated using the updated velocity model and the initial Q model. The updates lower the velocity at the shallow part, and as a result, the events in Figure 11 move up. Figure 11 also shows how some events (e.g. the flank of the right salt dome) become more coherent in phase after velocity updating. Figure 13 shows 10 representative ADCIGs of this migrated

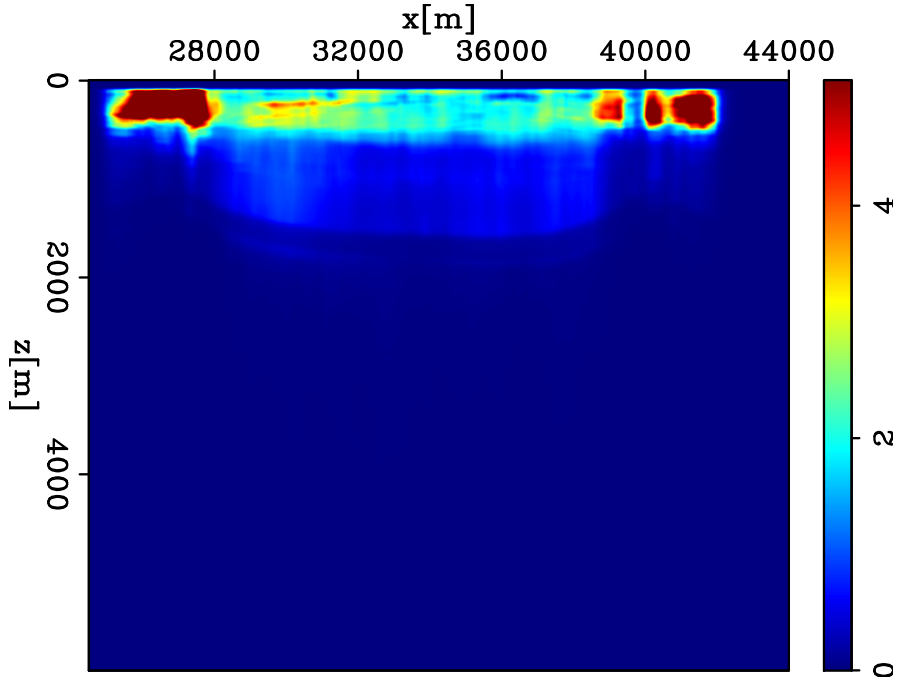

Figure 14: The velocity gradient of the first iteration of the inversion. [**CR**]

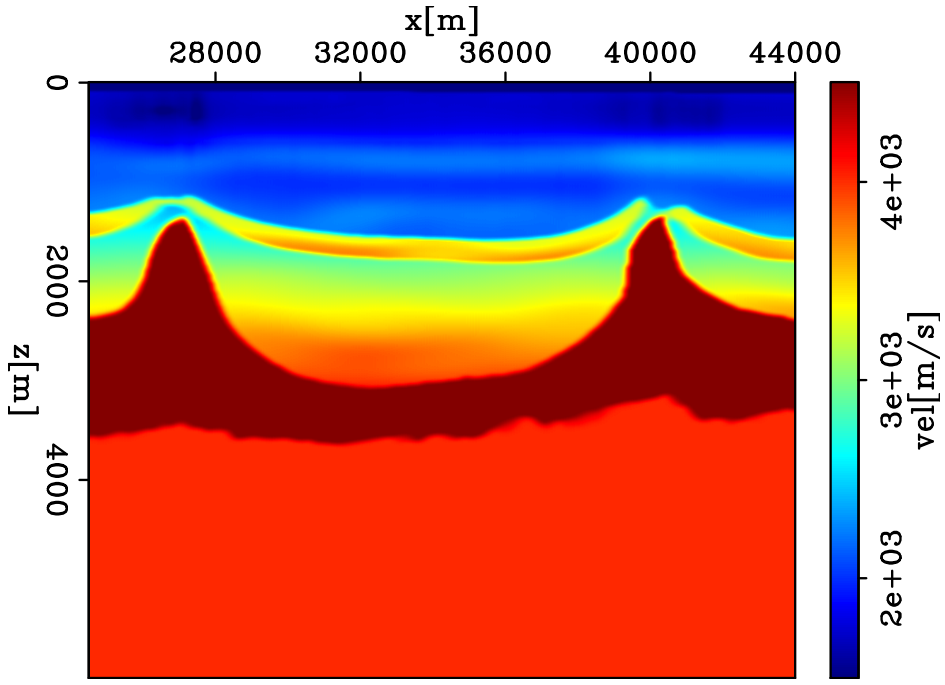

Figure 15: The updated velocity after 20 iterations. [**CR**]

image using the updated velocity model and the initial Q model. The decrease in the shallow velocity after inversion pushes the curves of the events in ADCIGs upward, and therefore flattens the gathers. Such flatness is significant above $z = 4,000$ m. More iterations or a different objective function may improve the flatness in a deeper depth; however, events below the base of salt ($z > 4,000$ m) are not the target of my study, and have little (if any) impact on the estimation of the shallow gas and channel for both the velocity and Q models. Because the Q model has not yet been updated, the dimming amplitudes in the seismic image have no improvements in Figure 11 and Figure 13.

During the final 20 iterations, I mainly focus on updating the Q model. Before Q updating, the seismic image (Figure 23) migrated using the updated velocity model and the initial Q model has only been compensated by the background Q value of 500. The image under the interpreted Q anomalies is wiped out. In my previous studies (Shen et al., 2013, 2014), I have shown that the parameter slope (ρ) is able to effectively quantify the attenuation effects from a seismic image. The slope value (ρ) can be computed from the logarithm of the spectral ratio between a measured spectra and a reference spectra (Tonn, 1991). The negative value of ρ means the image is undercompensated; while the positive value of ρ means the image is overcompensated. The larger the absolute value of ρ, the larger the Q effects measured from the seismic image, and the further the current Q model is from the accurate Q model – and vice versa. Therefore, the objective of this image-based Q inversion is to minimize the summation of $\rho(x;Q)$ over each image point. I have derived two objective functions to measure ρ from different image domains: (1) migrated image at zero subsurface offset (a postack objective function) and (2) ADCIGs (a prestack objective function). As described by Shen et al. (2013, 2014), inversion using a prestack objective function is able to produce a higher resolution and more accurate Q inversion results, although its computational cost is higher than the inversion using a poststack objective function.

To perform the inversion using a poststack objective function, I choose the trace at 33,880 m as the reference trace to compute ρ. This trace is far from both the shallow gas and the channel, and is assumed to be the least affected by the attenuation caused by these two Q anomalies. The window size to compute the spectra from the migrated image for ρ is 500 m in z direction and 125 m in x direction. I have developed an automatic picker to find the peak of the computed spectra over the wavenumber and record it as k_c. The desired wavenumber range that I choose to compute ρ is $[k_c - 0.015$ 1/m, $k_c + 0.015$ 1/m$]$. The velocity stretch effect in the migrated image is also corrected before spectral analysis for ρ.

Figure 16(a) is the logarithm of the spectral ratio from the attenuated image (Figure 23) between the window below the left Q anomaly in which the window center is at $x = 27,500$ m, $z = 2,500$ m and the reference window in which the window center is at $x = 33,880$ m, $z = 2,500$ m. Figure 16(b) is the logarithm of the spectral ratio from the attenuated image (Figure 23) between the window far from these two Q anomalies in which the window center is at $x = 34,500$ m, $z = 2,500$ m and the reference window in which the window center is at $x = 33,880$ m, $z = 2,500$ m. The

picked wavenumber range of these two locations is roughly within [0.005 1/m, 0.035 1/m]. Within this wavenumber range and regardless of the noisy wiggles, the curve in Figure 16(a) decreases linearly with wavenumber with a negative slope; while the curve in Figure 16(b) is almost flat with its slope value approximating to 0. These two slope values indicate the chosen window below the left Q anomaly is attenuated, and the chosen window far from these two Q anomalies has almost no attenuation. To remove the influence of the noise on the spectra shown as the wiggles, I use linear least-squares regression to fit a line to the curves of the logarithm of the spectral ratio within the picked wavenumber range by linear least squares regression. Figure 17 is the slope estimate of the image in Figure 23 for every image point used as the window center. The slope values at certain image points of the attenuated image in Figure 23 are positive. The possible reasons are because the chosen reference trace does not necessarily have the least attenuation impacts from the anomalies, and the way to pick the wavenumber range is not sophisticated enough. I clipped the positive numbers in Figure 17 to display the attenuated region only. The blue color in the slope map indicates the areas strongly attenuated. In accordance with the observation from Figure 23, two strong attenuation regions under the salt domes are highlighted by the blue in Figure 17. However, the blue regions below a 4 km depth are unexpectedly distributed, possibly because of the poor image quality below the base of salt. Fortunately, this deep part of the image has little impact on the estimation of the shallow Q anomalies.

Figure 18 is the inverted Q model displayed in logarithm scales ($\log_{10} Q$) after 20 iterations using the Q inversion with a poststack objective function. The results have two anomalies above the salt that are both shifted to the left of these two salt domes. The method using a poststack objective function has the disadvantage of producing a low-resolution result, which is part of the reason for the bias between an estimated location and the interpreted location of the anomalies. In addition, the right anomaly has a stronger attenuation than the left one, which contradicts the interpretation that the gas on the left has stronger attenuation than the right channel.

To perform the inversion using a prestack objective function (Shen et al., 2015), I choose the angle gather in which the midpoint is at 33,880 m as the reference gather to compute ρ, which is considered to be the least attenuated by two Q anomalies. This angle gather is referenced to the rest of the angle gathers to compute the slope. The window size to compute the spectra from the migrated image for ρ has only one direction along the depth with the length of 300 m. The smaller window size aims for a higher-resolution Q inversion results. The automatic picker for the desired wavenumber range is the same as in the method using a poststack objective function. The velocity stretch effect and angle stretch effect (Shen et al., 2015) in the ADCIGs are also corrected before spectral analysis for ρ.

The ADCIGs at the first iteration of inversion mainly for Q model updating have only been compensated by the background Q value of 500. Figure 19 displays the slope estimate of these 9 representative ADCIGs. Every point in the angle gathers are the center of the windows for computing the slope . The slope values at certain

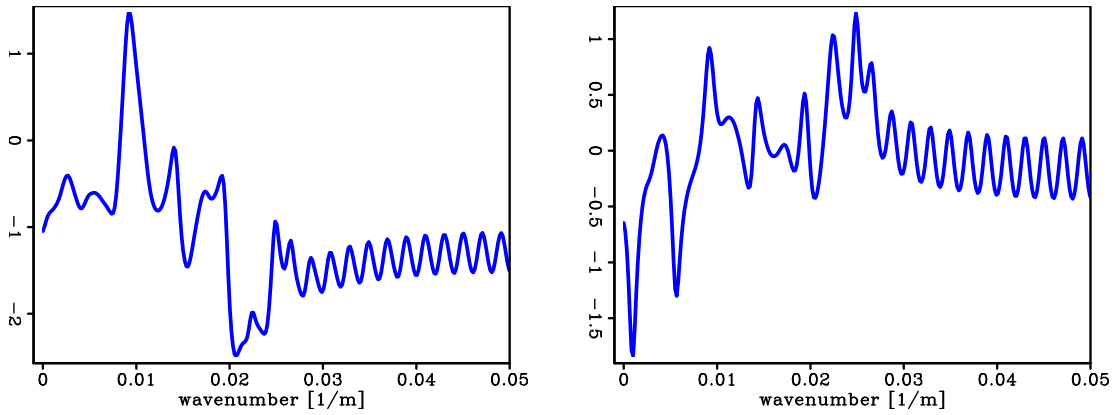

(a) (b)

Figure 16: (a) The logarithm of the spectral ratio from the attenuated image (Figure 23) between the window below the left Q anomaly in which the window center is at $x = 27,500$ m, $z = 2,500$ m and the reference window in which the window center is at $x = 33,880$ m, $z = 2,500$ m. (b) The logarithm of the spectral ratio from the attenuated image (Figure 23) between the window far from these two Q anomalies in which the window center is at $x = 34,500$ m, $z = 2,500$ m and the reference window in which the window center is at $x = 33,880$ m, $z = 2,500$ m. [**CR**]

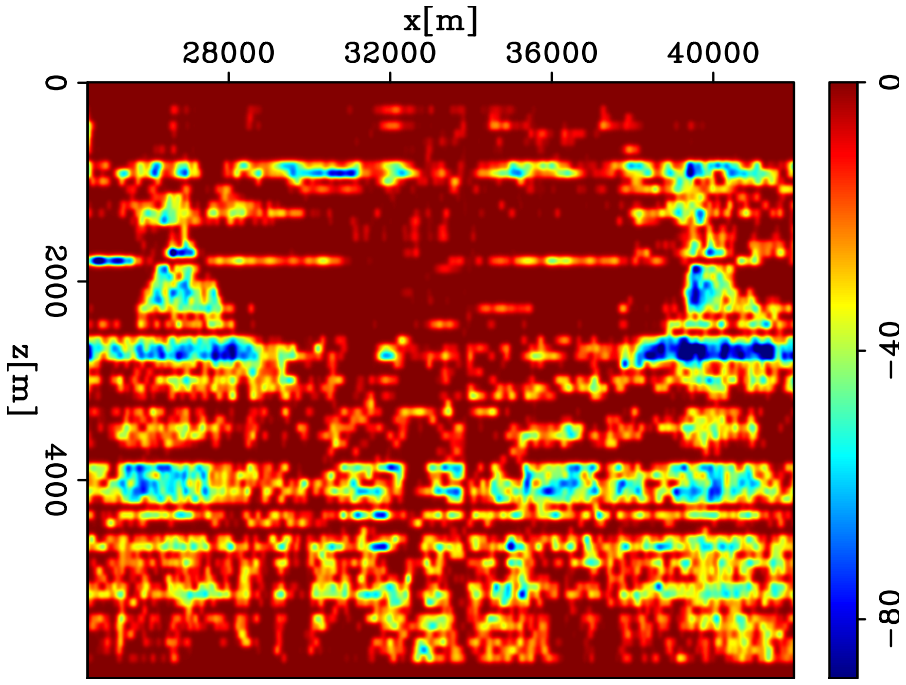

Figure 17: The slope estimate of the image in Figure 23 for every image point that is used as the window center. [**CR**]

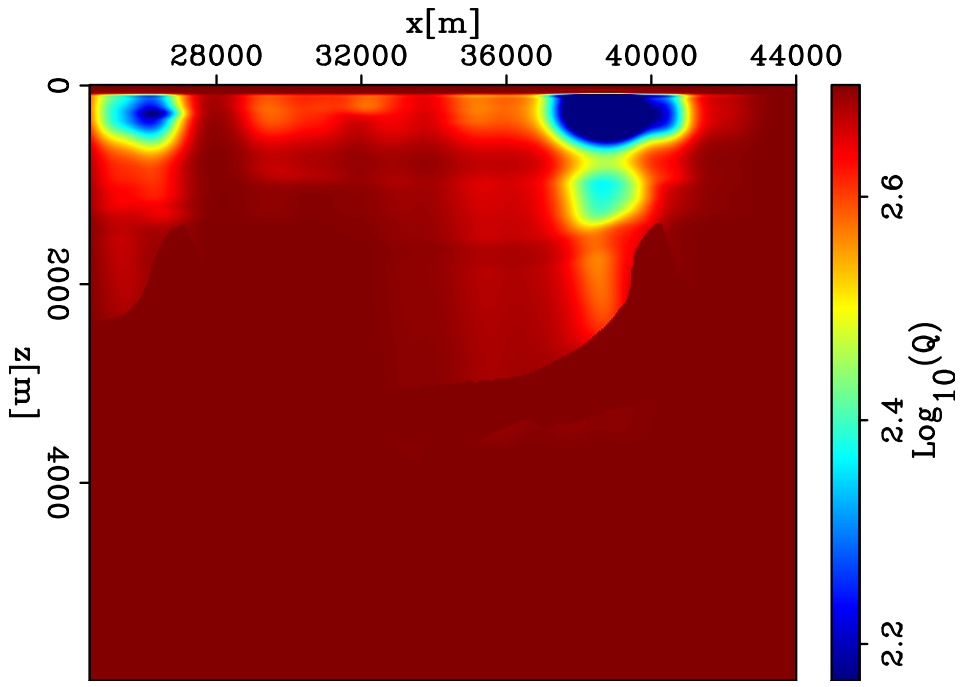

Figure 18: The inverted Q model displayed in logarithm scales ($\log_{10} Q$) after 20 iterations using the Q inversion with a poststack objective function. [**CR**]

points of the ADCIGs are positive because of the same reason previously described for the method using the poststack objective function. I clipped the positive number in Figure 19 to display the attenuated regions only. The blue color in the slope map indicates the strongly attenuated area. The blue colors are dominated at the depth below Q anomalies ($z < 1,500$ m) and above the base of the salt ($z > 4,000$ m). Again, the image below the base of the salt ($z > 4,000$ m) has little impact on the Q inversion. Therefore, I only focus the analysis below Q anomalies ($z < 1,500$ m) and above the base of salt ($z > 4,000$ m). With this depth range, the gathers in which the midpoint is far from the Q anomalies area (e.g., $x = 31$ km, $x = 33$ km and $x = 35$ km in Figure 28) have little attenuated region indicated by blue. As the midpoint moves closer to the Q anomalies (e.g., $x = 25$ km, $x = 29$ km and $x = 37$ km in Figure 28), the wave propagating at large angles passes through the Q anomalies; and therefore, the far angles at these ADCIGs are attenuated. Once the midpoint is at the anomalies area (e.g., $x = 27$ km, $x = 39$ km and $x = 41$ km in Figure 28), their near angles are attenuated. Figure 20 shows the zero-angle slope estimated measured from this attenuated ADCIGs with its blue color highlighting two strong attenuated regions within the salt domes.

Figure 21 shows the Q gradient at the first iteration of inversion mainly for Q model updating with a prestack objective function, in which the sign is opposite to the search direction. The gradient shows updates are strong around the shallow gas and channel region that exhibit the highest attenuation. Figure 22 is the inverted Q model displayed in logarithm scales ($\log_{10} Q$) after 20 iterations for Q inversion. The

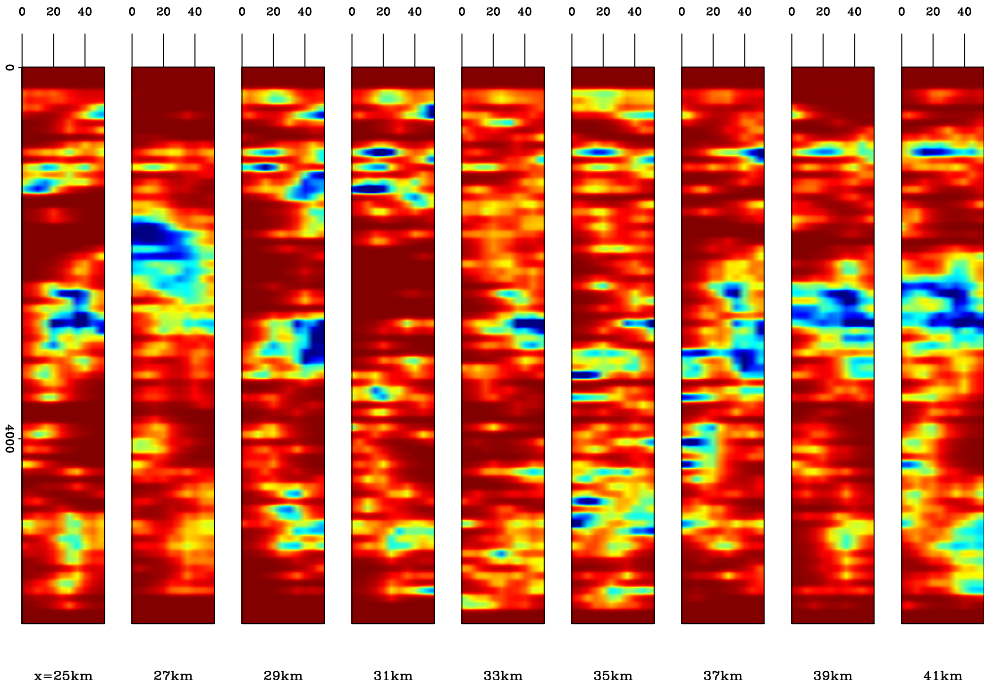

Figure 19: The slope estimate of the ADCIGs at the first iteration of inversion mainly for Q model updating. The slope estimates of 9 representative ADCIGs are displayed. Every point in the angle gathers are the center of the windows for computing the slope. [**CR**]

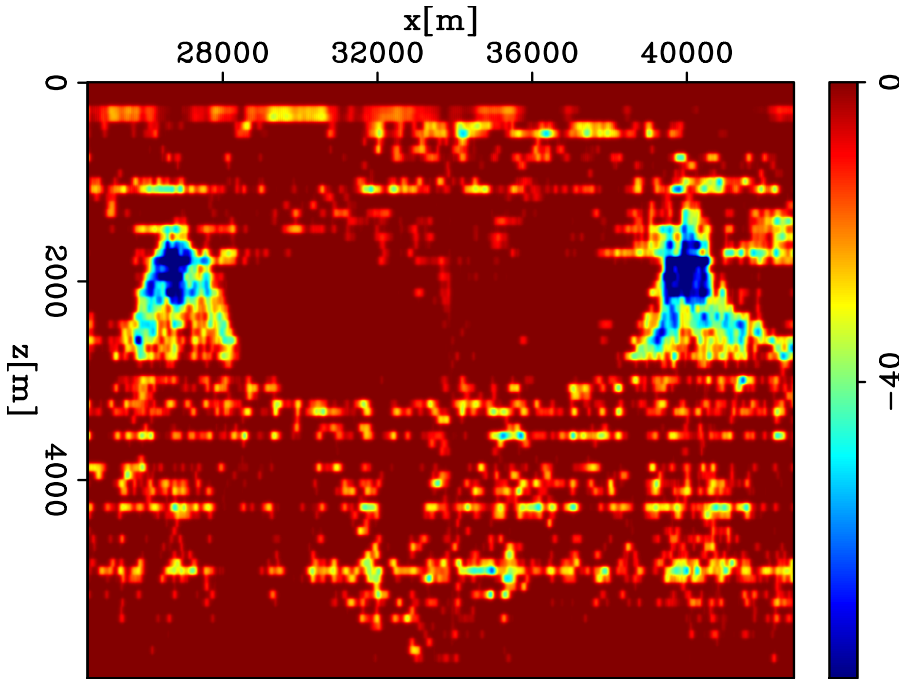

Figure 20: The slope estimate of the ADCIGs at the first iteration of inversion mainly for Q model updating. The slope estimates extracted at the zero angle are displayed. [**CR**]

inverted Q models recover two Q anomalies. The location and the relative shapes of such Q anomalies in Figure 22 match the interpretation much better than the ones in Figure 18. This result also proves the conclusion that the inversion using a prestack objective function has a better capability to build an accurate Q model than the one using a poststack objective function.

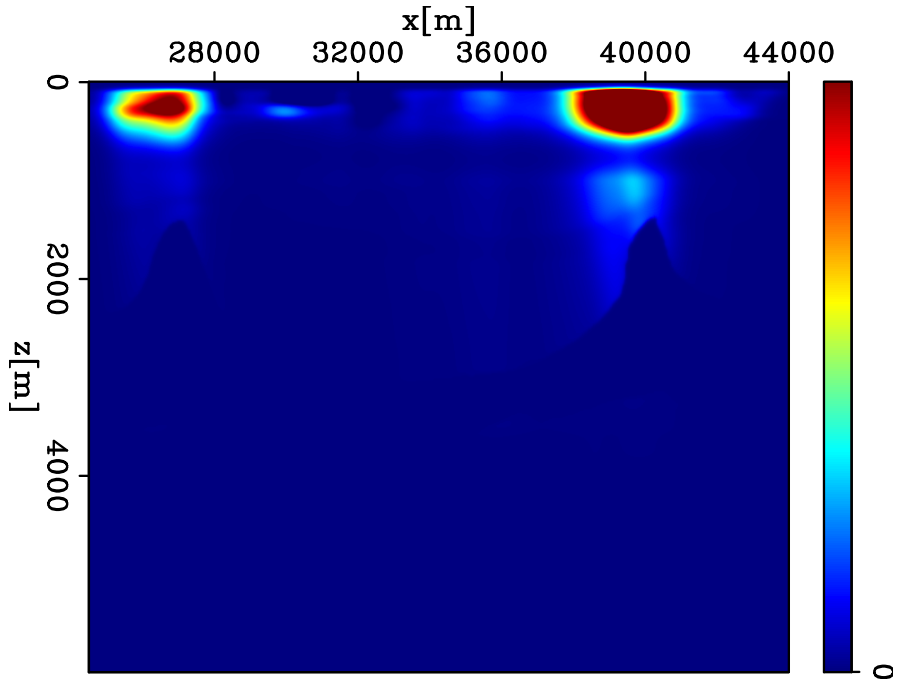

Figure 21: The Q gradient at the first iteration of inversion mainly for Q model updating, in which the sign is opposite to the search direction. [**CR**]

Figure 24 is the migrated image at zero subsurface offset using the updated velocity model and the inverted Q model. The structures at the gas and channel regions become brighter. These bright spots matches the interpretation that the strong impedance contact makes seismic reflection amplitudes strong. The compensated image below the Q anomalies in Figure 24 are improved in terms of their enhanced amplitudes and higher frequency content. To take a closer examination, I zoom in the region around the left and right of the salt peaks in Figure 25 and Figure 26, respectively. Figure 25(a) and 26(a) are the zoomed-in regions of the attenuated image in Figure 23. Figure 25(b) and 26(b) are the zoomed-in regions of the compensated image in Figure 24. Because the enhancement of the absolute amplitudes by Q compensation is already obvious in Figure 24, I apply Automatic Gain Control (AGC) to the zoomed-in regions in Figure 25 and Figure 26 to compare their frequency and phase improvements. The compensated images show that events become sharper because of the recovery of high frequencies and become more coherent because of attenuation-induced phase distortion being corrected. I compute the spectra of the events below the right Q anomaly of Figure 23 and Figure 24, and display them in the logarithm scale in Figure 27. The spectra shows the compensation with the inverted

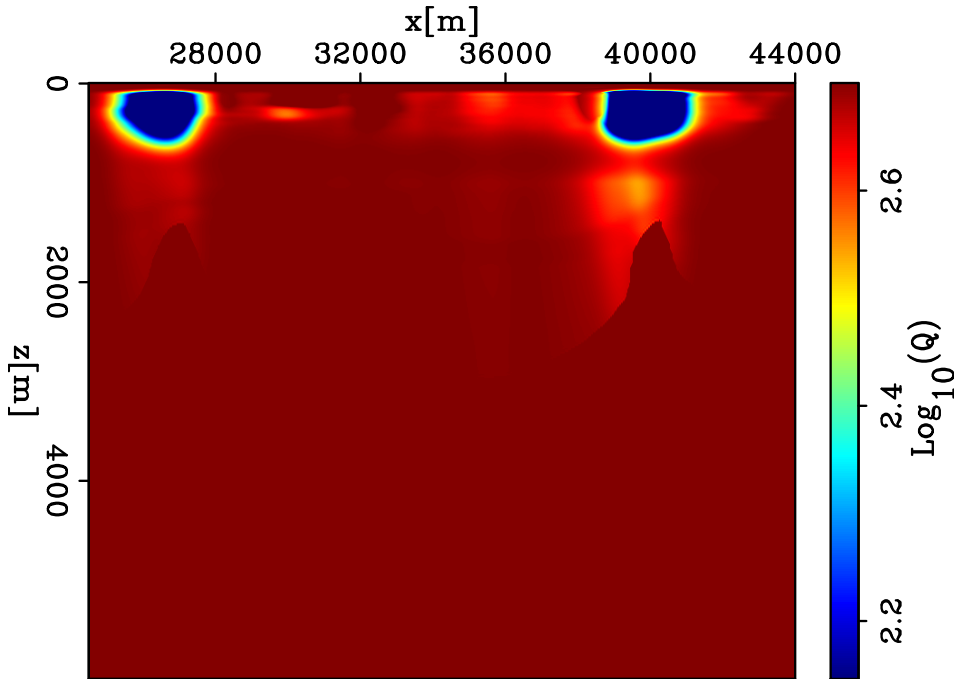

Figure 22: The inverted Q model displayed in logarithm scales ($\log_{10} Q$) after 20 iterations using the Q inversion with a prestack objective function. [**CR**]

Q model whitens the spectra and compensates for the higher frequency loss caused by attenuation.

Figures 28 and 29 show 10 representative ADCIGs of this migrated image with the Q model before and after Q updating, respectively. Results show the ADCIGs compensated by the inverted Q model have sharper and more coherent events. Such improvement brings benefit to the gather picking for velocity analysis and to AVO analysis for reservoir characterization.

CONCLUSION

The Dolphin's multi-client field data acquired in the North Sea used in this study has attenuation and velocity problems. Gas chimneys and channels exist in the subsurface with strong attenuation and low-interval velocity. In this paper, I first preprocessed this field data to regularize the bin grids and removed the swell noise, multiples, bubble and ghost. Then, I applied wave-equation migration velocity analysis to update the current velocity model. As a result, the velocity decreases in the gas and the channel area. The angle gathers migrated using the updated velocity model are much more flattened, and the events above the top of salt in the migrated images after velocity updating are more coherent. Then, I applied wave-equation migration Q analysis to invert for the Q models. The results show that the Q inversion using a prestack objective function better recovers the two Q anomalies than the Q inversion

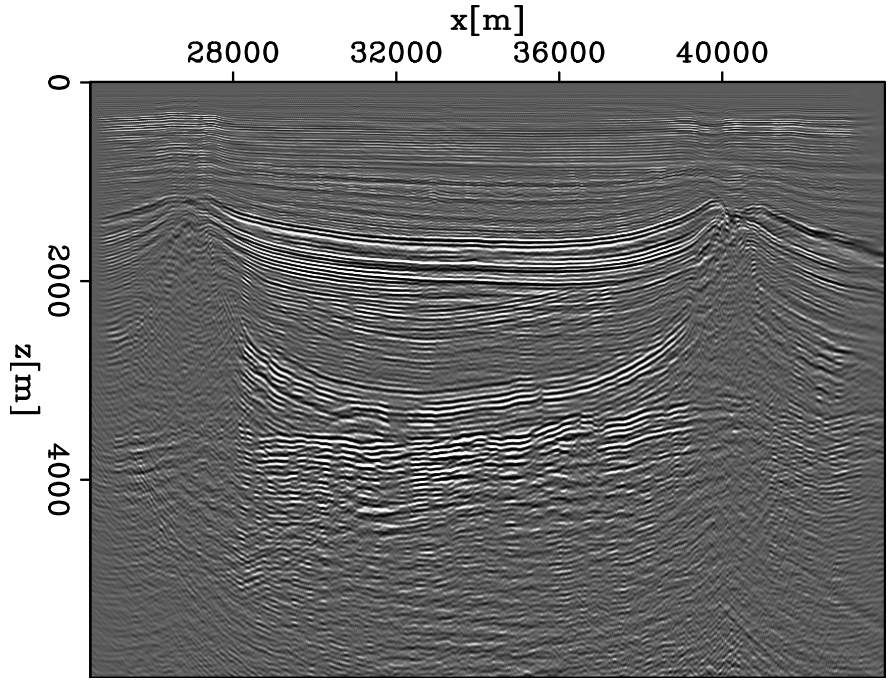

Figure 23: The migrated image at zero subsurface offset using the updated velocity model and the initial Q model. Same as Figure 11. Replicate the figure here for a convenient comparison with Figure 24. [**CR**]

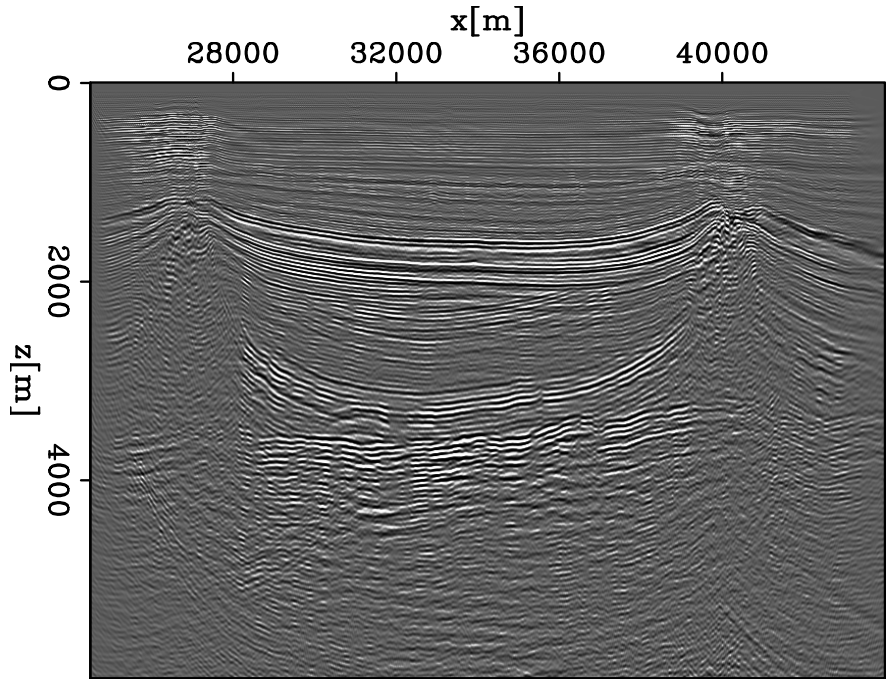

Figure 24: The migrated image at zero subsurface offset using the updated velocity model and the updated Q model. [**CR**]

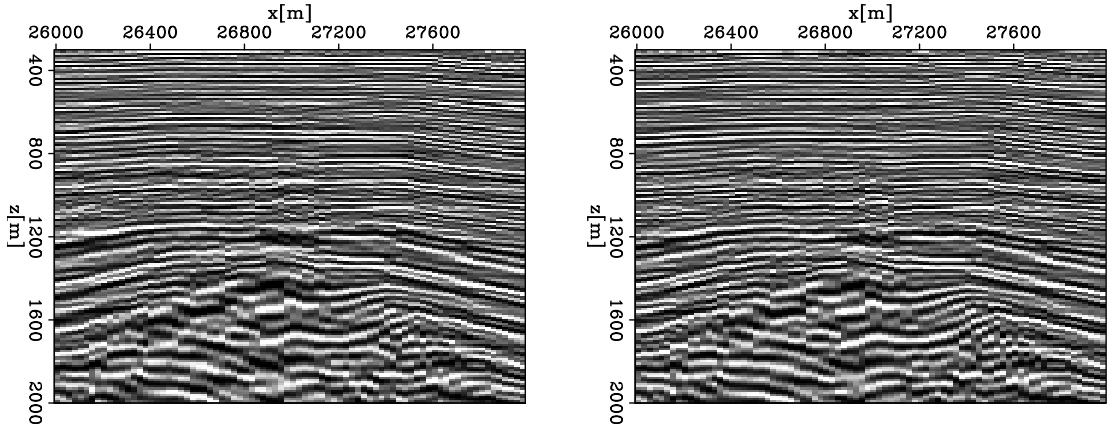

(a) (b)

Figure 25: Zoomed-in region around the left of the salt peak of (a) attenuated image in Figure 23 and (b) compensated image in Figure 24. AGC is applied to both images. [**CR**]

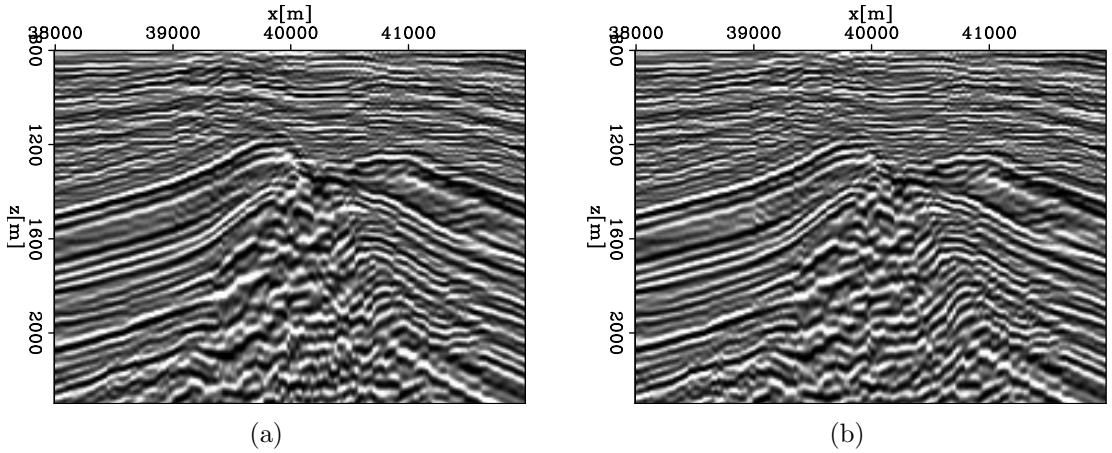

(a) (b)

Figure 26: Zoomed-in region around the right of the salt peak of (a) attenuated image in Figure 23 and (b) compensated image in Figure 24. AGC is applied to both images. [**CR**]

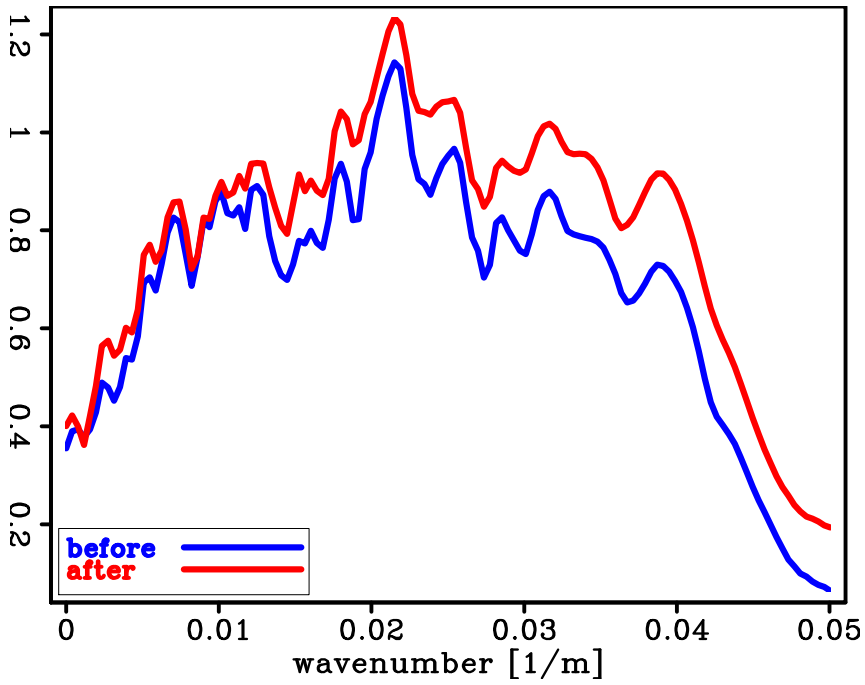

Figure 27: The spectra of the events below the right Q anomaly of Figure 23 and Figure 24. The spectra are displayed in the logarithm scale. [**CR**]

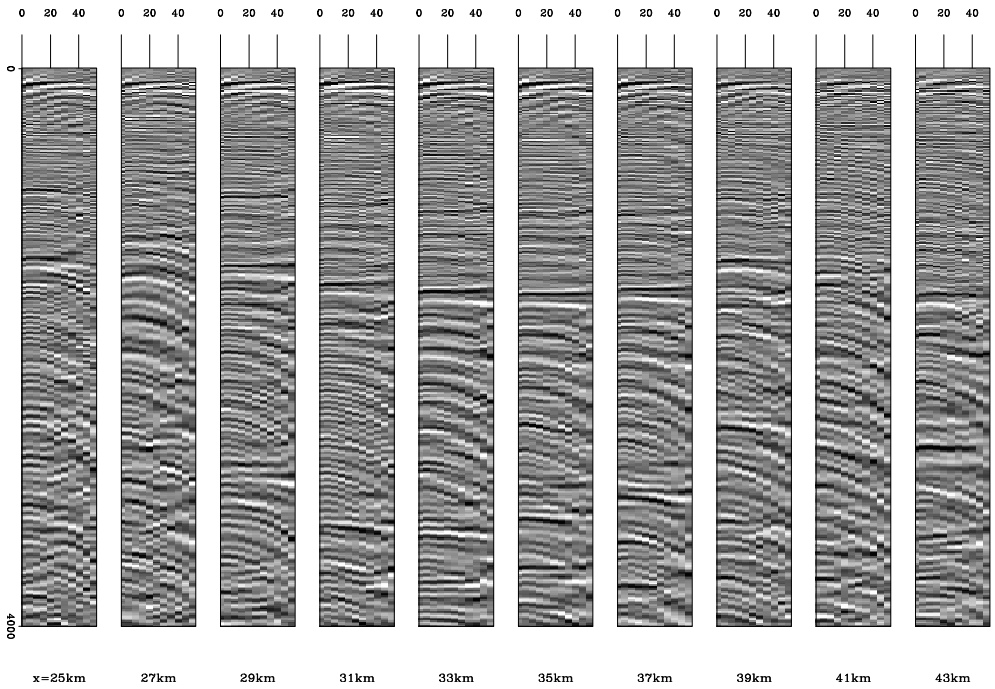

Figure 28: The ADCIGs using the updated velocity model and the initial Q model. AGC is applied. [**CR**]

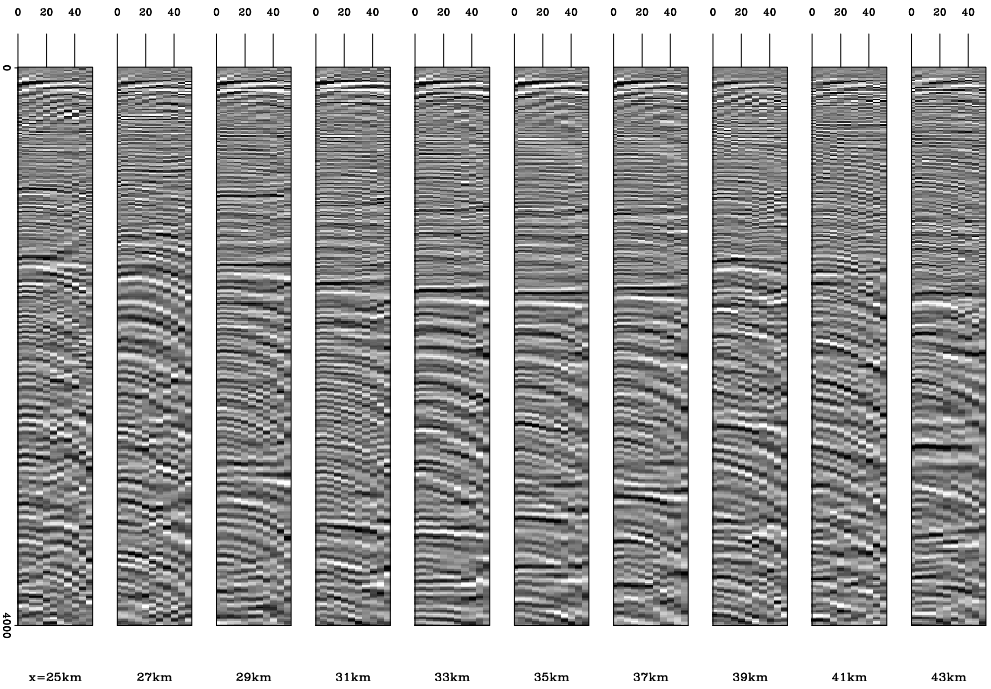

Figure 29: The ADCIGs using the updated velocity model and the inverted Q model. AGC is applied. [**CR**]

using a poststack objective function. The inverted Q model matches the interpretation quite well. Using this Q model in seismic migration, I made the seismic events below the anomalies clearly visible, with improved frequency content and coherency of the events.

ACKNOWLEDGMENTS

I would like to thank Dolphin Geophysical for providing these SHarp seismic data. I would also like to thank Biondo Biondi, Bob Clapp, Alejandro Cabrales, Gustavo Alves, Shuki Ronen, Stewart Levin, Jack Dvorkin, Ohad Barak, Taylor Dahlke for their helps and discussions.

REFERENCES

Clarebout, J. and S. Fomel, 2014, Geophysical image estimation by example.

Sava, P. and B. Biondi, 2004, Wave-equation migration velocity analysis-i: Theory: Geophysical Prospecting, **52**, 593606.

Shen, Y., 2015, Simultaneous inversion of velocity and q using wave-equation migration analysis: SEP-Report, **160**, 71–80.

Shen, Y., B. Biondi, and R. Clapp, 2015, Wave-equation based Q tomography from angle-domain common image gathers, 4334–4338.

Shen, Y., B. Biondi, R. Clapp, and D. Nichols, 2013, Wave-equation migration Q analysis (WEMQA): EAGE Workshop on Seismic Attenuation Extended Abstract.

———, 2014, Wave-equation migration Q analysis (WEMQA): SEG Technical Program Expanded Abstracts.

Shen*, Y., C. Willacy, and V. Goh, 2015, Image-based Q tomography using wavefield continuation in the presence of strong attenuation anomalies: A case study in gulf of mexico.

Tonn, R., 1991, The determination of seismic quality factor Q from VSP data: A comparison of different computational techniques: Geophysical Prospecting, **45**, 87–109.

Zhang, Y. and B. Biondi, 2013, Moveout-based wave-equation migration velocity analysis: Geophysics, **78**, U31–U39.